Materials Research Bulletin 94 (2017) 38–44

Contents lists available at ScienceDirect

Materials Research Bulletin

journal homepage: www.elsevier.com/locate/matresbu

Preparation of morphology-controlled TiO_2 nanocrystals for the excellent photocatalytic activity under simulated solar irradiation

Dandan Wang[a,b,c], Jinghai Yang[c,*], Xiuyan Li[c,*], Jian Wang[c], Jihui Lang[c], Jingshu Wang[c], Hang Song[a]

[a] Changchun Institute of Optics, Fine Mechanics and Physics, Chinese Academy of Sciences, Changchun 130033, PR China
[b] University of Chinese Academy of Sciences, Beijing 100049, PR China
[c] Key Laboratory of Functional Materials Physics and Chemistry of the Ministry of Education, Jilin Normal University, Siping 136000, PR China

ARTICLE INFO

Article history:
Received 7 February 2017
Received in revised form 11 May 2017
Accepted 11 May 2017
Available online 25 May 2017

Keywords:
Morphology-controlled
TiO_2
Nanocrystals
Photocatalysis

ABSTRACT

A simple synthetic approach based on solvothermal technique and hydrogenation was developed for preparation of TiO_2 nanocrystals with different morphologies such as elongated rhombic, dog-bone, oval and core-shell structured oval. The effect of oleic acid (OA) and oleylamine (OM) as two capping surfactants on the growth of TiO_2 nanocrystals was investigated. The physicochemical properties of the obtained samples were characterized by various techniques including TEM, XRD, UV–vis absorption, Raman, XPS, BET, PL and photocurrent measurement. In photodegradation of RhB under simulated solar irradiation, the oval-shaped TiO_2 nanocrystals with core-shell structure (co-TiO_2) was superior to other TiO_2 nanocrystals in catalytic activity. Moreover, the co-TiO_2 nanocrystals exhibited well recyclability during multiple photocatalytic tests. These excellent properties of co-TiO_2 were attributed to its special structure, including lattice-disordered surface layer and well-crystallized lattice core, and narrow band gap (2.67 eV).

1. Introduction

Eliminating the broad organic pollutants in water by using efficient semiconductor photocatalysts has attracted considerable attentions [1–3]. TiO_2 nanocrystals (NCs) are often cited as the best choice for energy materials due to these exceptional properties such as superior photocatalytic activity, thermally and chemically stability, environmental friendly and low cost, etc. [4–8]. These advantages originate from the unique physical and chemical properties of TiO_2 which depends not only on the crystal phase and particle size but also on the particle morphology [9–11]. Therefore, controlling the morphology of TiO_2 nanocrystals is of key importance in the fabrication of materials with desired photocatalytic properties.

Over the past decades, there are a number of synthetic routes to prepare TiO_2 NCs [12–14]. At present, conventional hydrolytic sol-gel process at relatively low temperature and nonhydrolytic process at elevated temperature are two main synthetic methods to prepare TiO_2 NCs. However, it is difficult to control the hydrolytic sol-gel process because its fast reaction rates, and slight changes in kinetics may lead to dramatic changes in size and morphology of the final materials [14]. Moreover, subsequent calcination is needed to induce crystallization of amorphous TiO_2 products in hydrolytic method, which increases the cost of production. For nonhydrolytic process, the use of oxygen donors other than water results in a drastic decrease in the reaction rate [15]. And nonhydrolytic process could directly produce monodisperse TiO_2 NCs with high crystallinity in general. But, a relatively low reaction rate of nonhydrolytic reactions limits the diversity in possible TiO_2 NCs morphology to a certain degree [16]. Consequently, the development about facile synthetic method of morphology −controlled TiO_2 NCs with high crystallinity remains a challenge.

Additionally, pure TiO_2 material with wide band gap (anatase ~3.2 eV; rutile ~3.0 eV) only utilizes ultraviolet irradiation which just accounts for five percent of the energy of the sunlight [17–19]. So, how to adequately take advantage of sunlight become significant issues for TiO_2 material in practical applications. There have been persistent efforts to increase the optical absorption of TiO_2 material [20–22]. One of the most efficient methods is generating donor or acceptor states in the band gap of TiO_2 by adding controlled metal or nonmetal impurities [23–26]. For example, nitrogen-doped TiO_2 has exhibited the favorable optical response to sunlight and superior photocatalytic activity owing to

* Corresponding authors.
E-mail addresses: jhyang1@jlnu.edu.cn (J. Yang), lixiuyan@jlnu.edu.cn (X. Li).

http://dx.doi.org/10.1016/j.materresbull.2017.05.029
0025-5408/

N 2p and O 2p states have been added and narrowed the band gap of TiO_2 [27]. Nevertheless, the photocatalytic activity of doped TiO_2 materials greatly depends on the characteristics and concentrations of dopant species, besides the method and its thermal and reductive treatment. Hence, it is difficult to prepare doped TiO_2 materials with desired band gap and optical absorption. At present, a novel TiO_2 material attracts considerable interest owing to narrow band gap and high photocatalytic activity under solar light irradiation [17,28]. Calcining for the long time under high pressure hydrogen condition has been confirmed as a way to prepare this novel TiO_2 material [29–32]. But, the high H_2-pressure process limits the method's wide application since hydrogen gas is highly flammable.

In this work, to tailored synthesize TiO_2 NCs, we adopted an alternative approach based on solvothermal technique and hydrogenation. TEM measurements of the obtained TiO_2 NCs demonstrated that they presented different morphologies such as elongated rhombic, dog-bone, oval and core-shell structured oval. Among all as-prepared TiO_2 NCs, the oval-shaped TiO_2 NCs with core-shell structure, including lattice-disordered surface layer and well-crystallized lattice core, presented a broader absorption to visible light owing to the narrower band gap (2.67 eV). The relationship between the morphology and photocatalytic activity of as-prepared TiO_2 NCs was investigated by the photocatalytic degradation of RhB under simulated solar irradiation.

2. Experimental

2.1. Chemicals

All the chemicals used in this experiment were of analytical grade and were used as received without further purification. Deionized water (resistivity >18.0 MΩ cm) was used throughout the experiments.

2.2. Synthesis of TiO_2 nanocrystals

TiO_2 NCs with different morphologies were synthesized according to a former research with some modification [16]. Typically, 5 mmol of tetrabutyl titanate (TBOT), 25 mmol of oleic acid (OA) and 25 mmol of oleylamine (OM) were added to a beaker including 100 mmol of absolute ethanol (TBOT/OA/OM = 1:5:5). The obtained mixture was stirred for 30 min before being transferred into a 100 mL Teflon-lined stainless-steel autoclave containing 20 mL of the azeotrope of ethanol and water. The system was then heated at 180 °C for 18 h. The obtained precipitates were washed for several times with ethanol and then dried at 60 °C for 6 h. Keeping the amount of TBOT, two other experiments with different ratios of TBOT/OA/OM (TBOT/OA/OM = 1:6:4 and 1:4:6) were carried out.

And then, the obtained TiO_2 product which synthesized under the condition of TBOT/OA/OM = 1:6:4 was calcined at 500 °C in low partial pressure H_2 for 2 h.

2.3. Characterization

TEM images and HRTEM images were recorded using a transmission electron microscopy (TEM, FEI Tenai G^2 F20). All X-ray diffraction (XRD) patterns were recorded on a D/max-2500 copper rotating-anode X-ray powder diffraction with Cu-Kα radiation of wavelength λ=1.5406 Å (40 kV, 200 mA). UV–vis absorption spectra were obtained on pellets of pressed powders using a Perkin-Elmer Lambda 900 spectrometer. Raman spectroscopy was measured by using Renishaw inVia Raman system under a 514.5 nm (or 2.41 eV) Ar + ion laser (20 mW) excitation. X-ray photoelectron spectra (XPS) were recorded on a Thermo Scientific ESCALAB 250×i A1440 system. Nitrogen sorption analysis was performed by a Nova l000 analyzer. The room temperature photoluminescence (PL) analysis was performed by using a Renishaw inVia micro-PL spectrometer (325 nm, He-Cd laser).

The photocurrent measurements were carried out by using a computer-controlled electrochemical work station (CHI-660C Instruments, China). A 300 W xenon lamp was used as light source. A standard three-electrode cell was used, which composed by the as-prepared samples coated on the indium-tin oxide glass (1.0 cm × 4.0 cm) as the working electrode, a saturated calomel electrode (SCE) as a reference and a platinum minigrid as a counter electrode. The supporting electrolyte was 0.5 M Na_2SO_4 solution. The photocurrent under chopped light irradiation was recorded at an applied potential of −0.5 V.

2.4. Photocatalytic degradation of Rhodamine B (RhB)

The photocatalytic performances of all as-prepared samples were evaluated by the photocatalytic decomposition of RhB aqueous solution. 50 mg of TiO_2 NCs was dispersed in 100 mL of RhB solution (7 mg/L). Prior to irradiation, the suspension was stirred in dark for 20 min to reach an adsorption-desorption equilibrium between the catalyst and RhB molecules. Subsequently, the suspension was irradiated using a solar simulator equipped with a Xe lamp (CEL-HXUV300 300 W 500 mW·cm^{-2}) filtered with a filter to reduce the fraction of UV photons. At every 15 min illumination interval, 2 mL of solution was drawn out and the solution was separated from the catalyst through centrifugation. The corresponding UV–vis spectra were recorded to determine the concentration of the remaining RhB by an UV–vis spectrophotometer (UV-5800PC, Shanghai Metash Instruments Co., Ltd). The photodegradation efficiency (%) of RhB was calculated from the following expression: the photodegradation efficiency of RhB (%) = $(C_0 - C_t)/C_0 \times 100\%$, where C_0 and C_t stands the initial concentration of RhB and the concentration of RhB at a real time, respectively. After washing with ethanol and deionized water for several times, the recycled catalyst was redispersed in 100 mL of RhB solution, and the new photocatalytic cycle began. The photocatalytic activity of Degussa P25 was also measured under the same conditions as reference.

3. Results and discussion

3.1. Morphology and phase structure

To synthesize TiO_2 NCs with different morphologies, the TBOT/OA/OM molar ratios were modulated and hydrogenation was adopted. The TEM images in Fig. 1 confirm the effect of a combination of OA and OM as well as hydrogenation on the morphology of TiO_2 NCs. When the TBOT/OA/OM mole ratio is 1:4:6, the elongated rhombic-shaped TiO_2 NCs (r-TiO_2) with a length of 60 nm and a width of 25 nm is obtained as presented in Fig. 1a. When the TBOT/OA/OM molar ratio is regulated to 1:5:5, it can be seen from Fig. 1b that the dog-bone-shaped TiO_2 NCs (d-TiO_2) is found to be 20 nm in length and 10 nm in width. When the TBOT/OA/OM molar ratio is further adjusted to 1:6:4, the oval-shaped TiO_2 NCs (o-TiO_2) is formed as shown in Fig. 1c. The lengths of major axis and the minor axis for o-TiO_2 NCs are 10 nm and 8 nm, respectively. The inserts in the top right-hand corner of Fig. 1a–c are HRTEM images corresponding to r-TiO_2, d-TiO_2 and o-TiO_2 NCs, the lattice fringe a spacing of 0.351 nm is clearly visible, which can be indexed to the (101) plane of anatase TiO_2 (JCPDS card No.21-1272). After calcining o-TiO_2 NCs in low partial pressure of H_2, the core-shell structured oval-shaped TiO_2 NCs (co-TiO_2) is obtained. As shown in Fig. 1d, the size of co-TiO_2 NCs is similar to that of o-TiO_2 NCs. But, there are obvious differences in morphology

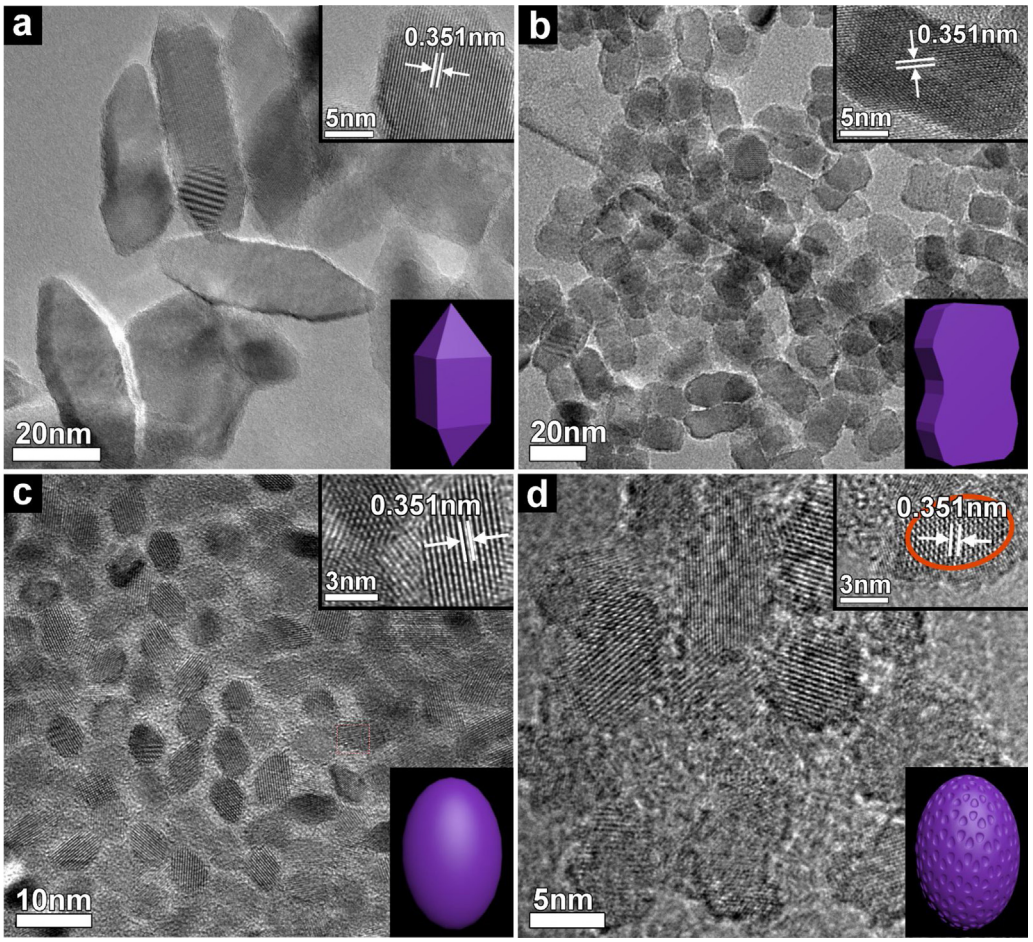

Fig. 1. TEM images of (a) r-TiO_2 NCs, (b) d-TiO_2 NCs, (c) o-TiO_2 NCs, and (d) co-TiO_2 NCs. The inserts on the top right corner of Fig. 1a–d are HRTEM images of different TiO_2 NCs, the inserts on the bottom right corner of Fig. 1a–d are schematic representations corresponding to different TiO_2 NCs.

between co-TiO_2 NCs and o-TiO_2 NCs. The co-TiO_2 NCs has unique core-shell structure including a disordered surface layer surrounding a crystalline core. As depicted in the orange circle of insert in Fig. 1d, the crystalline cores possess well resolved lattice fringes with spacing of about 0.351 nm which is in agreement with the (101) plane of anatase TiO_2 (JCPDS card No.21-1272) and the disordered outer layer is 1 ~ 2 nm in thickness.

XRD patterns of all as-prepared TiO_2 samples are shown in Fig. 2. The XRD patterns of r-TiO_2, d-TiO_2 and o-TiO_2 samples exhibit well-defined peaks assigned to the (101), (004), (200), (105), (211), (204), (116), (220) and (215) planes of the pure anatase phase (JCPDS card No. 21-1272), indicative of the high crystallinity of these samples. Compared to o-TiO_2 sample, the (004) diffraction peaks of r-TiO_2 and d-TiO_2 samples appear stronger and sharper, suggesting TiO_2 NCs evolves mainly along the [001] direction as the ratio of OA/OM ≤ 1 [16]. After hydrogenation treatment of o-TiO_2 sample, the diffraction peaks of obtained co-TiO_2 are similar to that of o-TiO_2 in form. No other peaks resulting from the presence of impurities are observed in the XRD pattern of co-TiO_2 sample.

3.2. Growth mechanism

The formation of TiO_2 follows two main steps that have been established: (i) the hydrolysis of titanium precursors to produce hydroxyalkoxides; (ii) subsequent condensation reactions to form a Ti-O-Ti network [16].The rates of these two processes must have a great influence on the morphology of TiO_2 NCs. In case studied here, an approach based on solvothermal technique was adopted. Its central features are that the water vapor is used as hydrolysis agent, and both OA and OM are chosen as important reagents to tune the morphology of TiO_2 NCs.

In this approach, TBOT first reacts with H_2O molecules to produce hydroxyalkoxide species that is the first step in the formation of TiO_2. In this step, the dosage of water is essential to control the morphology of final products. Here, instead of liquid water, water vapor reacts with TBOT. The azeotrope of ethanol and water can provide an appropriate amount of water vapor at

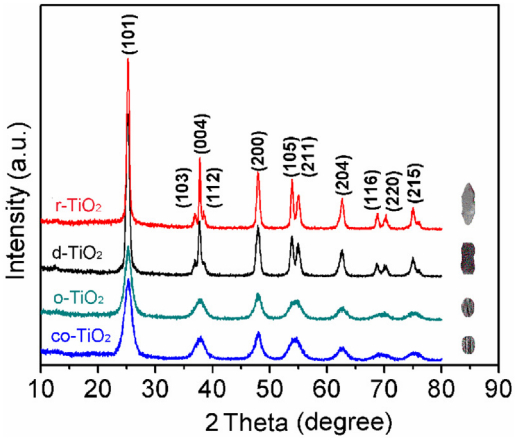

Fig. 2. XRD patterns of r-TiO_2, d-TiO_2, o-TiO_2 and co-TiO_2 NCs.

elevated temperature. Therefore, a slow hydrolysis rate is achieved. Afterwards, on the one hand, those hydroxyalkoxide precursors can react with each other through hydrolytic condensation, which is the second step in the formation of TiO_2; on the other hand, they can react with OA to form titanium carboxyalkoxide. The carboxyalkoxide with carboxylic chain can effectively hinder the attack of water molecules at metal centers [33,34]. As a result, the hydrolytic condensation is limited. It is worth noting that OM can promote the nonhydrolytic condensation process by aminolysis reaction with titanium carboxylalkoxide, which also is the second step in the formation of TiO_2 [13]. In summary, the reaction rate can be well regulated. In addition, OA and OM as capping agents tend to adhere on different faces of anatase, respectively [35]. OA binds strongly to the anatase {001} faces of TiO_2, whereas OM tends to adhere on the {101} faces of TiO_2. For above reasons, the morphology of TiO_2 NCs can be regulated by modulating the TBOT/OA/OM molar ratio. Three control experiments are performed. And the morphology evolution in range from 1:4:6 to 1:5:5 and 1:6:4 of the TBOT/OA/OM molar ratio is presented in Scheme 1. The TBOT/OA/OM mole ratios of 1:4:6, 1:5:5 and 1:6:4 correspond to r-TiO_2 NCs, d-TiO_2 NCs and o-TiO_2 NCs, respectively. Subsequently, the co-TiO_2 NCs featured with a well crystallized lattice core surrounded by a lattice-disordered shell was obtained in hydrogenation treatment. The disordered shell is believed to host the possible hydrogen dopant form the Ti–H and O—H bonds [30].

3.3. Optical and Raman propertiesOptical and raman properties

The UV–vis spectra of r-TiO_2, d-TiO_2, o-TiO_2 and co-TiO_2 NCs are given in Fig. 3a. It can be seen from Fig. 3a that r-TiO_2, d-TiO_2 and o-TiO_2 NCs are no absorbing toward the most part of the optical spectrum and exhibit a sharp absorption edge at ~400 nm. Interestingly, co-TiO_2 NCs presents a broader absorption range than other TiO_2 NCs, extending from ultraviolet light to visible light. The visual photographs of o-TiO_2 and co-TiO_2 powders are displayed in the inserts of Fig. 3a, where co-TiO_2 sample shows a totally black color that also indicates the enhanced light absorption, and the o-TiO_2 sample is purely white.

The band gaps are further calculated using the Tauc's relation given by:

$$\alpha h\boldsymbol{\nu} = K(h\boldsymbol{\nu} - \mathrm{E_g})^{0.5} \quad (1)$$

Where α is the absorption coefficient, $h\boldsymbol{\nu}$ is the photon energy and K is a material-dependent parameter [36]. Corresponding band gaps are estimated from the plots of $(\alpha h\nu)^2$ versus $h\nu$ considering direct allowed transitions for all samples. As presented in Fig. 3b, the band gaps are found to be about 3.19 eV for r-TiO_2, d-TiO_2 and o-TiO_2 NCs. And the band gap of co-TiO_2 NCs is about 2.67 eV. The smaller band gap of co-TiO_2 NCs can be attributed to the unique core-shell structure with a disordered surface layer surrounding a crystalline core [37]. The disordered surface layer is related to the occurrence of oxygen vacancies [37]. As shown in the insert of Fig. 3b, oxygen vacancies in disordered layer of co-TiO_2 NCs can

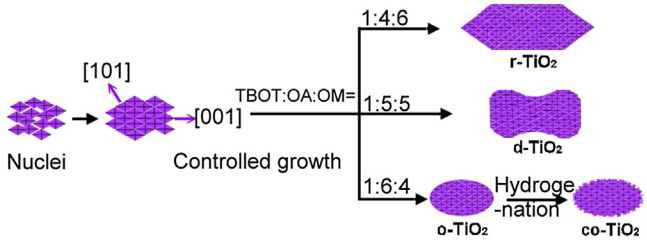

Scheme 1. Schematic representation showing the morphology evolution of TiO_2 NCs under different conditions.

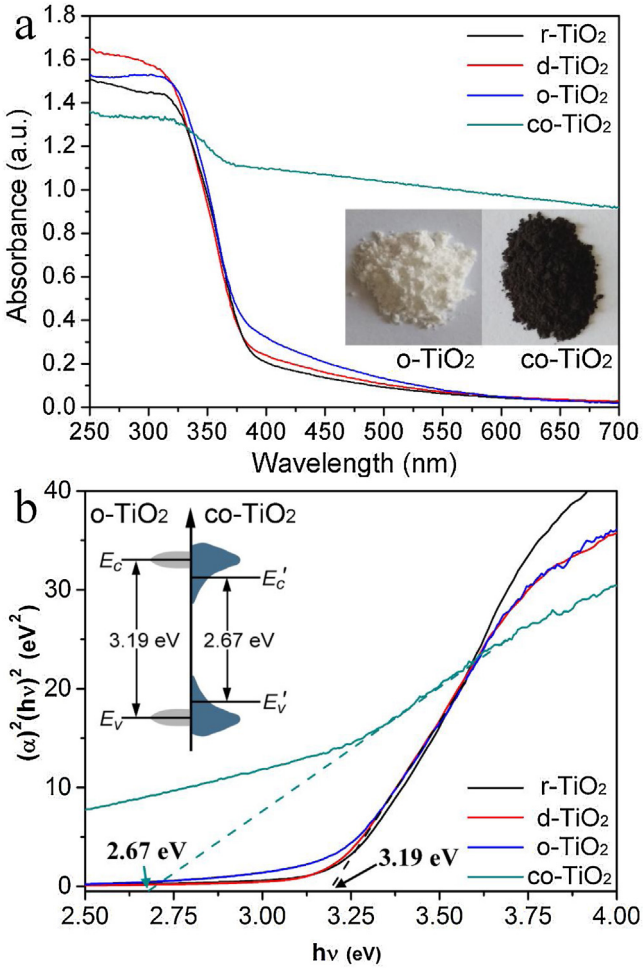

Fig. 3. (a) UV–vis spectra of r-TiO_2, d-TiO_2, o-TiO_2 and co-TiO_2 NCs; the inserts show the visual photographs of o-TiO_2 and co-TiO_2 powders. (b) Corresponding band gap width of different TiO_2 NCs by tangent method; the inserts are illustrations of electronic density of states of o-TiO_2 NCs and co-TiO_2 NCs.

contribute to the mid gap states and crease broadened tails of states extending into the otherwise forbidden band gap [28,38]. As a result, co-TiO_2 NCs has a narrow band gap and presents a broader absorption to visible light.

Raman spectroscopy is a spectroscopic technique to measure molecular vibrations. It was recorded to examine structural differences in o-TiO_2 and co-TiO_2 NCs. Anatase TiO_2 belongs to D4 h 19 (I41/amd) space groups which has distinctive characteristics in Raman spectra [4]. As shown in Fig. 4, the four main peaks at 149.3, 397.5, 515.1 and 639.0 cm^{-1} are detected in both Raman spectra of investigated samples, which can be assigned to the typical anatase bands of Eg, B1 g, A1 g and Eg, respectively [39]. Compared to the Raman spectrum of o-TiO_2 NCs, the significant blue-shift and broadening of the Eg (144 cm^{-1}) peak for co-TiO_2 NCs demonstrates that the original symmetry of TiO_2 lattice is broken down. It can be attributed to the surface disorder in co-TiO_2 NCs. This kind of lattice disorder results from phonon confinement or nonstoichiometry. And oxygen vacancy in lattice-disordered surface layer of co-TiO_2 NCs should be the main reason for the blue-shift and broadening of the Raman peak [40].

3.4. Bonding environment

XPS was performed to investigate the surface composition and bonding environment of the o-TiO_2 and co-TiO_2 NCs. Fig. 5a

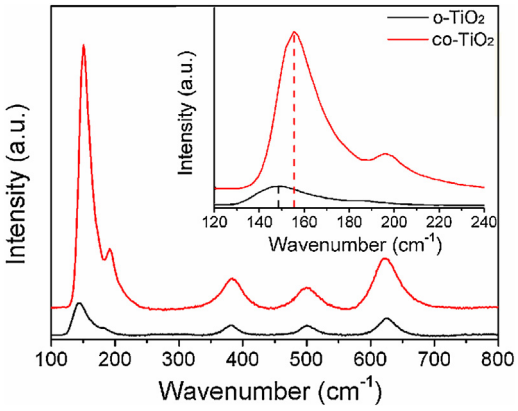

Fig. 4. Raman spectra of o-TiO_2 and co-TiO_2 NCs.

presents typical XPS spectra of o-TiO_2 and co-TiO_2 NCs. There are no other peaks except for Ti, O, and C. The C 1 s peak at 284.6 eV results from the adventitious carbon-based contaminant. The XPS spectra of titanium ion for o-TiO_2 and co-TiO_2 NCs are given in Fig. 5b, two peaks at 457.2 and 463.1 eV are corresponding with Ti 2p3/2 and 2p1/2 peaks of the typical Ti^{4+} species in TiO_2, respectively. The Ti-O-Ti peak is observed at 528.5 eV in O1 s XPS spectra (Fig. 5c). Compared with o-TiO_2 NCs, the weakened Ti-O-Ti peak of co-TiO_2 NCs is attributed to the enormous oxygen vacancies in co-TiO_2 [8]. In addition, the other broad O 1 s peak can be resolved into two peaks centered at 530.8 eV and 532.3 eV, which confirms the presence of Ti-O species and free −OH bonding on the surface, respectively [39]. The intensity of peak at 532.3 eV for co-TiO_2 NCs is higher than that of o-TiO_2 NCs. This can be attributed to the oxygen-defective sites in co-TiO_2 NCs that tend to bind with hydrogen atoms and formed more hydroxyl surface groups [39].

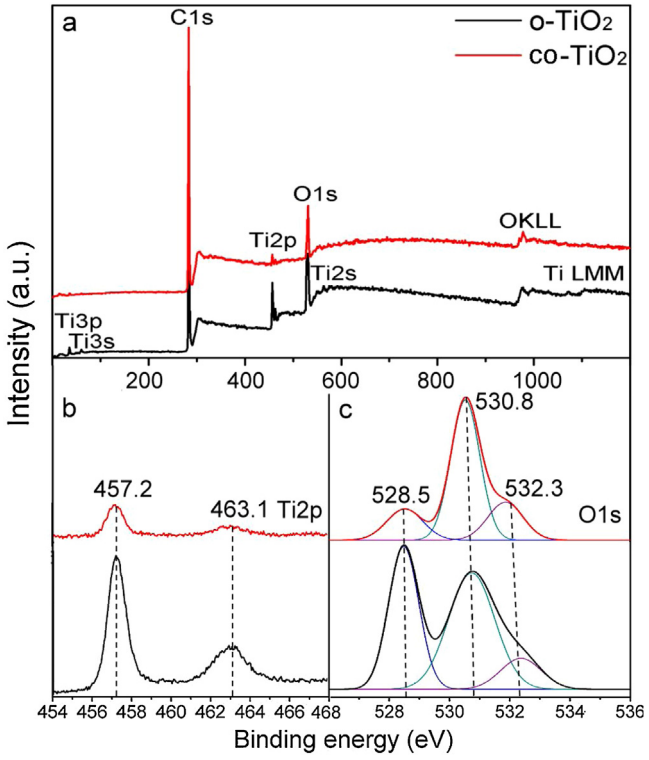

Fig. 5. (a) The survey scan of XPS of o-TiO_2 and co-TiO_2 NCs. (b) Ti 2p XPS spectra of XPS of o-TiO_2 and co-TiO_2 NCs. (c) O 1 s XPS spectra of XPS of o-TiO_2 and co-TiO_2 NCs.

3.5. Photocatalytic, photoelectric and PL properties

To investigate the photocatalytic activities of all as-prepared TiO_2 NCs, the photodegradation efficiency of RhB as a function of simulated solar irradiation time was recorded. As shown in Fig. 6a, the decomposition rate of RhB by co-TiO_2 is 96.76% after 90 min, while the photodegradation efficiencies of r-TiO_2, d-TiO_2, o-TiO_2 and P25 are 44.32%, 65.72%, 81.37% and 36.89%, respectively. The blank test (without catalyst) shows the photolysis of RhB is extremely slow (4.50%). Based on the above photocatalytic results, the photocatalytic activities follow the order co-TiO_2 > o-TiO_2 > d-TiO_2 > r-TiO_2 > P25. This is the same as the order of specific surface area of all samples, which are obtained from nitrogen sorption analysis. The specific surface area of all samples as follows: 109.74 $m^2 g^{-1}$ (co-TiO_2), 96.38 $m^2 g^{-1}$ (o-TiO_2), 71.76 $m^2 g^{-1}$(d-TiO_2), 62.82 $m^2 g^{-1}$ (r-TiO_2) and 52.48 $m^2 g^{-1}$ (P25). The larger specific surface area correlates with more exposed active sites of catalyst that is one reason for above difference in photocatalytic activity [41]. Moreover, it can be seen from TEM images (Fig. 1) that co-TiO_2 and o-TiO_2 NCs possess a smaller size than other samples. Smaller TiO_2 NCs can give rise to the quantum confinement effects that benefit to the separation of photogenerated carriers [42–44]. This is a reason why co-TiO_2 and o-TiO_2 NCs have superior photocatalytic property.

In addition, the first order kinetic equation $\ln(C_0/C) = kt$ is used to fit the experimental data in Fig. 6b, where k is the apparent rate constant. The k value for co-TiO_2 (0.0359 min^{-1}) is the biggest

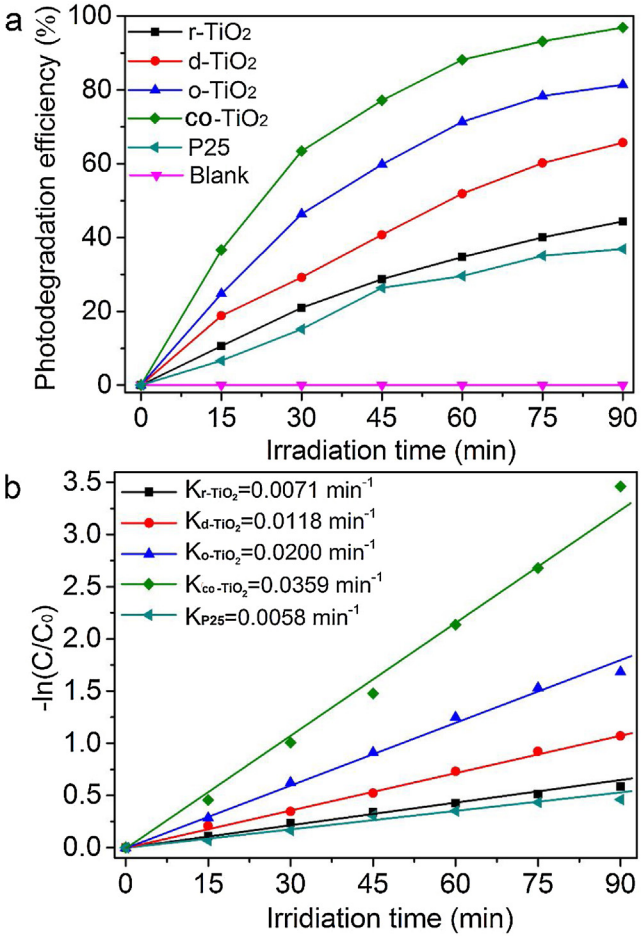

Fig. 6. (a) Photocatalytic decolouration of RhB under simulated solar irradiation with various catalysts. (b) The relationship curves of $\ln(C_0/C)$ versus reaction time for the different photocatalysts.

among all tested samples, which is about 1.8 times that of o-TiO_2 NCs (0.0200 min^{-1}). In addition to the larger specific surface area, narrow band gap (2.67 eV) is main factor for the excellent photocatalytic activity of co-TiO_2 NCs. Scheme 2 shows the possible photocatalytic mechanisms for o-TiO_2 and co-TiO_2 NCs under simulated solar irradiation. In comparison with o-TiO_2 NCs which only utilizes ultraviolet that just accounts for five percent of the energy of the sunlight, the co-TiO_2 NCs can make full use of the sunlight due to the broader absorption to visible light; Moreover, when the photo-generated electrons return to holes, oxygen vacancy sites in co-TiO_2 NCs can trap the electrons and keep the hole to electron spacing [17]. Then, more photogenerated carriers can interact with the surrounding species to form reactive oxygen species (ROS: $\cdot O^{2-}$, ·OH,). Accordingly, it is not difficult to understand why co-TiO_2 NCs exhibit better photocatalytic activity than o-TiO_2 NCs.

The lower recombination efficiency of the photo-induced carriers for co-TiO_2 NCs can be evaluated from the PL emission. Both o-TiO_2 and co-TiO_2 NCs present a similar PL pattern shape as presented in Fig. 7a. The PL signals are due to excitonic PL, which basically result from surface oxygen vacancies and defects of as-prepared TiO_2 NCs [45]. The peaks at 500.49 and 541.82 nm are ascribed attributed to band edge free excitons, and other peak at 587.21 nm is attributed to band edge free excitons [46]. The excitonic PL intensity of co-TiO_2 NCs is lower than that of o-TiO_2 NCs, which indicates the lower recombination probability of the photo-induced electron-hole pairs. This result illustrates that the mid gap states in co-TiO_2 NCs induced by oxygen vacancies facilitate the separation of charges [46,47]. The photocurrent response tests further confirm above result. As shown in Fig. 7b, the current density of co-TiO_2 NCs is obviously higher than that of o-TiO_2 NCs. The relatively high current density fully proves there are more photo-generated carriers in co-TiO_2 NCs.

To test the recyclability of co-TiO_2 NCs, we repeat the photocatalytic experiments with the same sample for six times, using filtration to separate the photocatalyst from solution after each test. After filtering, the as-prepared co-TiO_2 NCs give a recovery ratio of approximately 92%. And the decomposition rate of RhB has no significant reduction during multiple photocatalytic experiments as shown in Fig. 8. These results indicate co-TiO_2 NCs have good recyclability and stable photocatalytic performance in the suspension system.

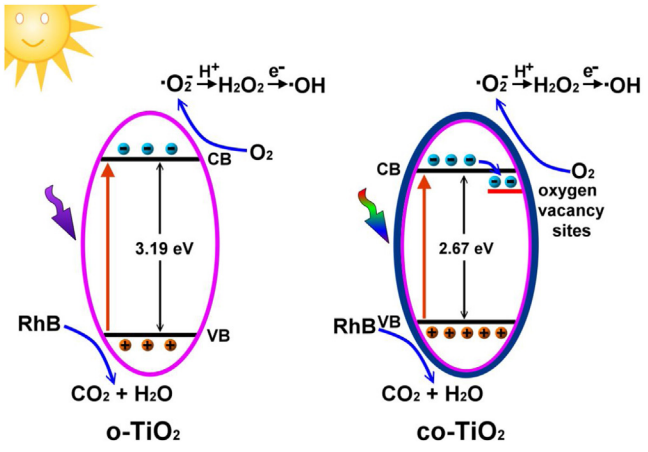

Scheme 2. The possible mechanisms for photocatalytic degraded RhB over o-TiO_2 and co-TiO_2 NCs under simulated solar irradiation.

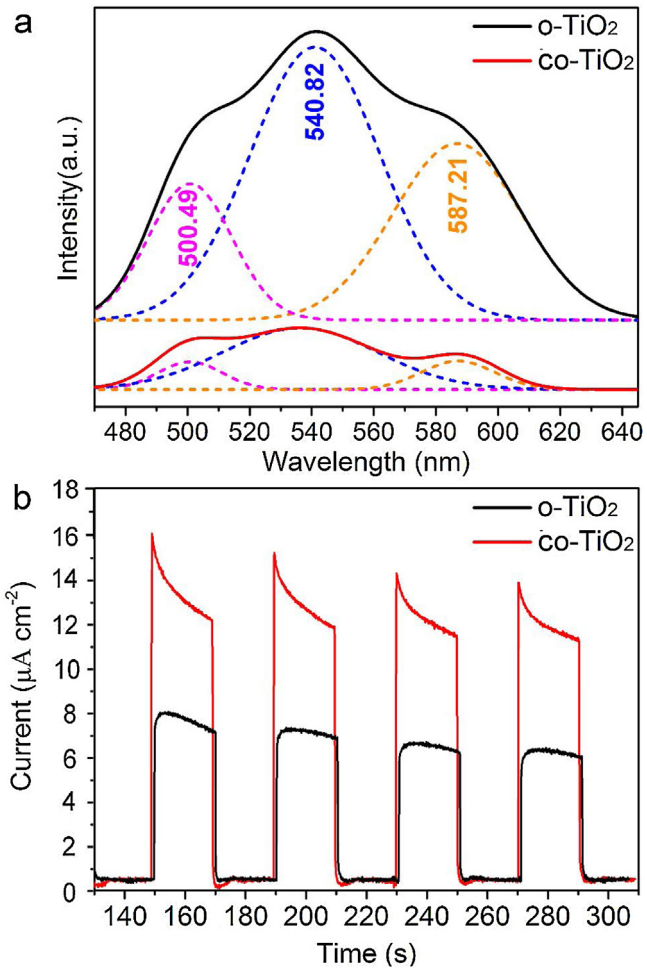

Fig. 7. (a) PL spectra and (b) photocurrent response of o-TiO_2 and co-TiO_2 samples.

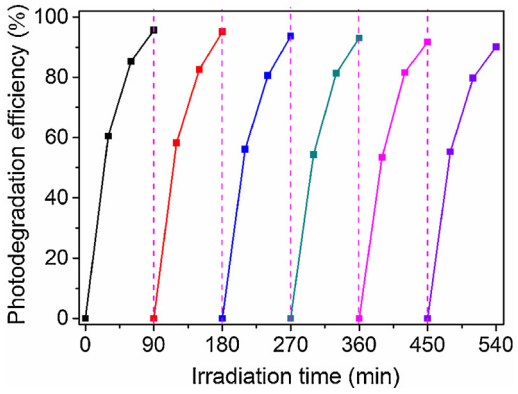

Fig. 8. The reusability of co-TiO_2 NCs for RhB decoloration.

4. Conclusions

In summary, we demonstrated the preparation of monodisperse TiO_2 nanocrystals (NCs) with various morphologies, such as elongated rhombic, dog-bone, oval and core-shell structured oval, by using modified approach based on solvothermal technique and hydrogenation. The morphology of TiO_2 was controlled by changing oleic acid/oleylamine molar ratio, and the corresponding growth mechanism was explained. The study of photocatalytic activity under simulated solar irradiation indicated oval-shaped TiO_2 NCs with core-shell structured (co-TiO_2) possessed the best

activity among all samples. The excellent activity of co-TiO_2 can be mainly attributed to its narrow band gap (2.67 eV) and lower recombination probability of the photo-induced electron-hole pairs. Subsequently, cyclic test confirmed the co-TiO_2 NCs had stable photocatalytic activity and recyclability. Based on the optical absorption to visible light, the co-TiO_2 NCs will have promising application in large-scale photocatalytic reactions in industries.

Acknowledgments

This work is supported by the National Natural Science Foundation of China (Grant Nos. 61378085, 51479220, 11404137, 51608226 and 61308095), Program for the development of Science and Technology of Jilin province (Item No. 20130102004JC, 201215222 and 20140101205JC).

References

[1] M. Azarang, A. Shuhaimi, R. Yousefi, S.P. Jahromi, One-pot sol-gel synthesis of reduced graphene oxide uniformly decorated zinc oxide nanoparticles in starch environment for highly efficient photodegradation of methylene blue, RSC Adv. 5 (2015) 21888–21896.
[2] H.R. Azimi, M. Ghoranneviss, S.M. Elahi, M.R. Mahmoudian, F. Jamali-Sheini, R. Yousefi, Excellent photocatalytic performance under visible-light irradiation of ZnS/rGO nanocomposites synthesized by a green method, Front. Mater. Sci. 10 (2016) 385–393.
[3] A. Kharatzadeh, F.J. Sheini, R. Yousefi, Excellent photocatalytic performance of Zn(1-x)MgxO/rGO nanocomposites under natural sunlight irradiation and their photovoltaic and UV detector applications, Mater. Des. 107 (2016) 47–55.
[4] X. Chen, L. Liu, F. Huang, Black titanium dioxide (TiO_2) nanomaterials, Chem. Sho. Rev. 44 (2015) 1861–1885.
[5] R. Sedghi, S.A.B. Heidari, M.M. Heravi, TiO_2/polymeric supported silver nanoparticles applied as superior nanocatalyst in reduction reactions, Mater. Res. Bull. 92 (2017) 65–73.
[6] S.M. Taha, M.E. Amer, A.M. Elmarsafy, M.Y. Elkady, J.M. Chovelon, Degradation of boscalid by nitrogen-doped/undoped TiO_2 and persulfate ions using different activation conditions and the identification of its main degradation products using LC/MS/MS, Chem. Eng. J. 288 (2016) 845–857.
[7] M. Sohail, H.L. Xue, Q.Z. Jiao, H.S. Li, K. Khan, S.S. Wang, Y. Zhao, Synthesis of well-dispersed TiO_2@reduced graphene oxide (rGO) nanocomposites and their photocatalytic properties, Mater. Res. Bull. 90 (2017) 125–130.
[8] M.C. Wu, I.C. Chang, K.C. Hsiao, W.K. Huang, Highly visible-light absorbing black TiO_2 nanhorystals synthesized by sol-gel method and subsequent heat treatment in low partial pressure H_2, J. Taiwan Inst. Chem. Eng. 63 (2016) 430–435.
[9] Q.K. Xi, G. Han, M.S. Jin, Z.X. Xie, L.S. Zheng, Synthesis of titania nanosheets with a high percentage of exposed (001) facets and related photocatalytic properties, J. Am. Chem. Sho. 131 (2009) 3152–3153.
[10] Y.Q. Dai, C.M. Cobley, J. Zeng, Y.M. Sun, Y.N. Xia, Synthesis of anatase TiO_2 nanhorystals with exposed {001} facets, Nano Lett. 9 (2009) 2455–2459.
[11] L.X. Lin, J.T. Huang, X.F. Li, M.A. Abass, S.W. Zhang, Effective surface disorder engineering of metal oxide nanocrystals for improved photocatalysis, Appl. Catal. B: Environ. 203 (2017) 615–624.
[12] P.H. Mutin, A. Vioux, Nonhydrolytic prhoessing of oxide-based materials: simple routes to control homogeneity, morphology, and nanostructure, Chem. Mater. 21 (2009) 582–596.
[13] A. Sandoval, R. Zanella, T.E. Klimova, Titania nanotubes decorated with anatase nanocrystals as support for active and stable gold catalysts for CO oxidation, Catal. Today 282 (2017) 140–150.
[14] K. Kanie, T. Sugimoto, Shape control of anatase TiO_2 NCs by amino acids in a gel-sol system, Chem. Commun. 158 (2004) 4–158 (5).
[15] J.N. Hay, H.M. Raval, Synthesis of organic-inorganic hybrids via the non-hydrolytic sol-gel prhoess, Chem. Mater. 13 (2001) 3396–3403.
[16] C.T. Dinh, T.D. Nguyen, F. Kleitz, T.O. Do, Shape-controlled synthesis of highly crystalline titania nanhorystals, ACS Nano 3 (2009) 3737–3743.
[17] X.B. Chen, L. Liu, P.Y. Yu, S.S. Mao, Increasing solar absorption for phothoatalysis with black hydrogenated titanium dioxide nanhorystals, Science 331 (2011) 746–749.
[18] X.K. Zeng, Z.Y. Wang, N. Meng, D.T. McCarthy, A. Deletic, J.H. Pan, X.W. Zhang, Highly dispersed TiO_2 nanocrystals and carbon dots on reduced graphene oxide: ternary nanocomposites for accelerated photocatalytic water disinfection, Appl. Catal. B: Environ. 202 (2017) 33–41.
[19] J.W. Shi, Z.Y. Wang, C. He, G.D. Li, C.M. Niu, Carbon-doped titania flakes with an hotahedral bipyramid skeleton structure for the visible-light photocatalytic mineralization of ciprofloxacin, RSC Adv. 5 (2015) 98361–98365.
[20] L.G. Devi, R. Kavitha, A review on plasmonic metal-TiO_2 composite for generation trapping, storing and dynamic vectorial transfer of photogenerated electrons across the schottky junction in a photocatalytic system, Appl. Surf. Sci. 360 (2016) 601–622.
[21] R. Marschall, L. Wang, Non-metal doping of transition metal oxides for visible-light phothoatalysis, Catal. Today 225 (2014) 111–135.
[22] J. Mu, B. Chen, M. Zhang, Z. Guo, P. Zhang, Z. Zhang, Y. Sun, C. Shao, Y. Liu, Enhancement of the visible-light Photocatalytic activity of In_2O_3-TiO_2 nanofiber heteroarchitectures, ACS Appl. Mater. Interfaces 4 (2012) 424–430.
[23] X. Jiang, X. Fu, L. Zhang, S. Meng, S. Chen, Photocatalytic reforming of glycerol for H_2 evolution on Pt/TiO_2: fundamental understanding the effect of co-catalyst Pt and the Pt deposition route, J. Mater. Chem. A 3 (2015) 2271–2282.
[24] T. Liu, H. Zhang, Novel Fe-doped anatase TiO_2 nanosheet hierarchical spheres with 94% {001} facets for efficient visible light photodegradation of organic dye, RSC Adv. 3 (2013) 16255–16258.
[25] C. Wang, Z. Chen, H. Jin, C. Cao, J. Li, Z. Mi, Enhancing visible-light photoelectrhohemical water splitting through transition-metal doped TiO_2 nanorod arrays, J. Mater. Chem. A 2 (2014) 17820–17827.
[26] P. Zhang, Y. Yu, E. Wang, J. Wang, J. Yao, Y. Cao, Structure of nitrogen and zirconium Co-doped titania with enhanced visible-light photocatalytic activity, ACS Appl. Mater. Interfaces 6 (2014) 4622–4629.
[27] R. Asahi, T. Morikawa, T. Ohwaki, K. Aoki, Y. Taga, Visible-light photocatalysis in nitrogen-doped titanium oxides, Science 293 (2001) 269–271.
[28] T. Xia, X. Chen, Revealing the structural properties of hydrogenated black TiO_2 nanhorystals, J. Mater. Chem. A 1 (2013) 2983–2989.
[29] H. Cui, W. Zhao, C. Yang, H. Yin, T. Lin, Y. Shan, Y. Xie, H. Gu, F. Huang, Black TiO_2 nanotube arrays for high-efficiency photoelectrhohemical water-splitting, J. Mater. Chem. A 2 (2014) 8612–8616.
[30] L. Liu, P.Y. Yu, X. Chen, S.S. Mao, D.Z. Shen, Hydrogenation and disorder in engineered black TiO_2, Phys. Rev. Lett. 111 (2013) 1–5.
[31] D.H. Wang, L. Jia, X.L. Wu, L.Q. Lu, A.W. Xu, One-step hydrothermal synthesis of N-doped TiO_2/C nanhoomposites with high visible light photocatalytic activity, RSC Nanoscale 4 (2012) 576–584.
[32] X. Yu, B. Kim, Y.K. Kim, Highly enhanced photoactivity of anatase TiO_2 nanhorystals by controlled hydrogenation-induced surface defects, ACS Catal. 3 (2013) 2479–2486.
[33] J. Joo, S.G. Kwon, T. Yu, M. Cho, J. Lee, J. Yoon, T. Hyeon, Large-scale synthesis of TiO_2 nanorods via nonhydrolytic sol-gel ester elimination reaction and their application to photocatalytic inactivation of E. coli, J. Phys. Chem. B 109 (2005) 15297–15302.
[34] Y. Jun, M.F. Casula, J.H. Sim, S.Y. Kim, J. Cheon, A.P. Alivisatos, Surfactant-assisted elimination of a high energy facet as a means of controlling the shapes of TiO_2 nanhorystals, J. Am. Chem. Sho. 125 (2003) 15981–15985.
[35] B.H. Wu, C.Y. Gou, N.F. Zheng, Z.X. Xie, G.D. Stucky, Nonaqueous production of nanostructured anatase with high-energy facets, J. Am. Chem. Sho. 130 (2008) 17563–17567.
[36] R. Khanam, D. Taparia, B. Mondal, D. Mohanta, Black titania: effect of hydrogenation on structural and thermal stability of nanotitania, Appl. Phys. A 122 (2016) 1–7.
[37] A. Naldoni, M. Allieta, S. Santangelo, M. Marelli, F. Fabbri, S. Cappelli, C.L. Bianchi, R. Psaro, V.D. Santo, Effect of nature and lhoation of defects on bandgap narrowing in black TiO_2 NCs, J. Am. Chem. Sho. 134 (2012) 7600–7603.
[38] S.G. Ullattil, P. Periyat, A 'one pot' gel combustion strategy towards Ti^{3+} self-doped 'black' anatase TiO_{2-x} solar phothoatalyst, J. Mater. Chem. A 4 (2016) 5854–5858.
[39] J. Chen, Z. Ding, C. Wang, H. Hou, Y. Zhang, C. Wang, G. Zou, X. Ji, Black anatase titania with ultrafast sodium-storage performances stimulated by oxygen vacancies, ACS Appl. Mater. Interfaces 8 (2016) 9142–9151.
[40] T. Leshuk, R. Parviz, P. Everett, H. Krishnakumar, R.A. Varin, F. Gu, Photocatalytic activity of hydrogenated TiO_2, ACS Appl. Mater. Interfaces 5 (2013) 1892–1895.
[41] T.R. Gordon, M. Cargnello, T. Paik, F. Mangolini, R.T. Weber, P. Fornasiero, C.B. Murray, Nonaqueous synthesis of TiO_2 nanhorystals using TiF_4 to engineer morphology oxygen vacancy concentration, and photocatalytic activity, J. Am. Chem. Sho. 134 (2012) 6751–6761.
[42] D.D. Wang, J.H. Yang, X.Y. Li, H.J. Zhai, J.H. Lang, H. Song, Preparation of magnetic Fe_3O_4@SiO_2@mTiO_2-Au spheres with well-designed microstructure and superior photocatalytic activity, J. Mater. Sci. 51 (2016) 9602–9612.
[43] P.V. Kamat, Quantum dot solar cells. semiconductor nanocrystals as light harvesters, J. Phys. Chem. C 112 (2008) 18737–18753.
[44] J.K. Mwaura, X. Zhao, H. Jiang, K.S. Schanze, J.R. Reynolds, Spectral broadening in nanocrystalline TiO_2 solar cells based on poly(p-phenylene ethynylene) and polythiophene sensitizers, Chem. Mater. 18 (2006) 6109–6111.
[45] J. Niu, S. Shen, L. Zhou, Z. Liu, P. Feng, X. Ou, Y. Qiang, Synthesis and hydrogenation of anatase TiO_2 microspheres composed of porous single crystals for significantly improved photocatalytic activity, RSC Adv. 6 (2016) 62907–62910.
[46] Q. Xiang, K. Lv, J. Yu, Pivotal role of fluorine in enhanced photocatalytic activity of anatase TiO_2 nanosheets with dominant (001) facets for the photocatalytic degradation of acetone in air, Appl. Catal. B: Environ. 96 (2010) 557–564.
[47] H. Wu, J. Ma, Y. Li, C. Zhang, H. He, Photocatalytic oxidation of gaseous ammonia over fluorinated TiO_2 with exposed (001) facets, Appl. Catal. B: Environ. 152–153 (2014) 82–87.